

Structure of cosmic web in non-linear regime: the nearest neighbour and spherical contact distributions

Mohammad AnsariFard¹, Zahra Baghkhan¹, Laya Ghodsi^{1,2}, Sina Taamoli^{1,3}, Farbod Hassani⁴, Shant Baghram¹ 

¹ Department of Physics, Sharif University of Technology, P. O. Box 11155-9161, Tehran, Iran

² Department of Physics and Astronomy, University of British Columbia, Vancouver, BC, V6T 1Z1, Canada

³ Department of Physics and Astronomy, University of California, Riverside, CA 92521, USA

⁴ Institute of Theoretical Astrophysics, University of Oslo, 0315 Oslo, Norway

Accepted XXX. Received YYY; in original form ZZZ

ABSTRACT

In non-linear scales, the matter density distribution is not Gaussian. Consequently, the widely used two-point correlation function is not adequate anymore to capture the matter density field's entire behaviour. Among all statistics beyond correlation functions, the spherical contact and nearest neighbour distribution function seem promising tools to probe matter distribution in a non-linear regime. In this work, we use halos from cosmological N -body simulations and galaxy groups from the volume-limited galaxy group catalogues to compare the spherical contact distribution function with the nearest neighbour distribution function. We also calculate the J-function for different samples. Moreover, we consider the redshift evolution and mass-scale dependence of statistics in the simulations and dependence on the magnitude of volume-limited samples in group catalogues. The shape of the spherical contact probability distribution function is nearly skew-normal, with skewness and kurtosis being approximately 0.5 and 3, respectively. On the other hand, the nearest neighbour probability distribution function is nearly log-normal, with logarithmic skewness and kurtosis being approximately 0.1 and 2.5, respectively. Accordingly, the spherical contact distribution function probes larger scales compared to the nearest neighbour distribution function, which is influenced by details of structures. We also find a linear relation between the first and second moment of the spherical contact probability distribution function in simulations, which could be used as a distinguishing probe of cosmological models.

Key words: (cosmology:) large-scale structure of the Universe – (cosmology:) dark matter – galaxies: statistics

1 INTRODUCTION

The standard model of cosmology is deduced from the early and late time statistics of matter and radiation distribution in the Universe. The two-point correlation function and its wide usage in cosmology are well known. As an example, cosmologists employed the two-point correlation function in the early time Cosmic Microwave Background (CMB) fluctuations (Aghanim et al. 2020; Hinshaw et al. 2013) and the late time Large Scale Structure (LSS) data sets (Sanchez et al. 2012; Wang et al. 2013; Shi et al. 2016; Alam et al. 2017; Ivanov et al. 2020). The main advantage of the two-point correlation function is in its easy procedure to compare theory with observations. It is used to find the cosmological parameters (Alam et al. 2017; Abbott et al. 2018) or even to find a deviation from

the standard model of cosmology and to constrain the inflationary models (Akrami et al. 2020). In Fard & Baghram (2018) some of us studied the specific features (oscillatory and step-function) of the primordial power spectrum and their imprints on early and late-time two-point correlation functions.

The study of the LSS in non-linear scales is essential as it is tightly connected to the essence of dark matter. The small scale challenges of cold dark matter de Martino et al. (2020) could be a hint beyond the standard model of cosmology. The distribution of the dark matter halos and sub-halos in small scales is crucial to test cosmological models. This distribution can be studied by their gravitational effects Baghram et al. (2011); Li et al. (2012); Rahvar et al. (2014); Feldmann & Spolyar (2015) or/and the distribution of satellite galaxies Agustsson & Brainerd (2018).

As a result of mode coupling in strongly non-linear scales, the matter density distribution is far from Gaussian (Bernardeau et al. 2002).

* baghram@sharif.edu

To extract all data's information, we need to investigate statistics, which depend on all higher-order correlations. In this direction, several methods and different quantities have been proposed. The first choice is to study the higher-order n -point correlation functions, directly (Scoccimarro et al. 1998; Verde & Heavens 2001; Sefusatti et al. 2006). However, in strongly non-linear scales, it is compelling to introduce new approaches to extract information from data while reducing computational costs. Two approaches are considered to study cosmological structure formation: continuous random field and discrete point processes.

In the context of continuous random field process, the topological structure of the cosmic web has been explored through the genus statistics of iso-density contours (Gott III et al. 1986; Hamilton et al. 1986; Melott 1990) and the Minkowski functionals (Schmalzing & Buchert 1997). In this direction, the genus statistics is used to constrain the cosmological parameters (Gott III et al. 2008; Appleby et al. 2018; Colley & Gott 2015), to test modified gravity theories (Wang et al. 2012), and dark energy models (Zunckel et al. 2011).

In the second approach, which is the main focus of this work, we consider the matter density as a discrete point process consists of particles, halos, or galaxies. In these methods, one can calculate the statistical quantities by counting the number of objects. The relation between these quantities and the n -point correlation functions shows that they depend on all order correlations. So, they contain more information than the two-point correlation function, especially at small scales (White 1979; Bernardeau 1992; Balian & Schaeffer 1989; Szapudi & Szalay 1993).

The number of objects in a specific volume such as a sphere is called counts-in-cells (CIC) (Hubble 1936; Zwicky 1957; Balian & Schaeffer 1989). We know that in small scales, the distribution of CIC or equivalently one-point probability of the matter density field is not Gaussian and follows approximately a log-normal distribution (Coles & Jones 1991; Ueda & Yokoyama 1996). The nearly log-normal behaviour of the cosmic matter density field is a feature of evolving perturbations from the linear Gaussian inflationary initial conditions (Guth 1981; Linde 1982) to the late time non-linear and non-Gaussian distribution. Accordingly, it is informative to investigate the shape of the probability distribution of the matter density field and its evolution (Lam & Sheth 2008; Bernardeau et al. 2014; Uhlemann et al. 2016; Ivanov et al. 2019; Repp & Szapudi 2020b; Mandal & Nadkarni-Ghosh 2020). It is worth mentioning that other interesting ideas such as an Edgeworth expansion, skewness, and kurtosis analysis are argued in this field of study (Colombi 1994; Gaztanaga et al. 2000; Shin et al. 2017; Klypin et al. 2018; Einasto et al. 2020). On large scales, the CIC contains the same information as the two-point correlation function. But there is more information encoded in the log-normal shape of the CIC distribution on small scale. Accordingly, the cosmological dependence of the CIC statistics is interesting to be explored in mildly and strongly non-linear regimes from an observational and theoretical point of view. Uhlemann et al. (2020) showed that the measured CIC statistics are sensitive to the cosmological parameters and neutrino mass. Repp & Szapudi (2020a) used the CIC to break the degeneracy between σ_8 and galaxy bias. Also, it is employed to study the primordial non-Gaussianity in LSS by measuring the f_{NL} parameter Friedrich et al. (2020). Recently, Jamieson & Loverde (2020) introduced an approach to use a position-dependent one-point distribution of matter density as a cosmological observable. Besides all this progress, there are some limitations. The results depend on the size and shape of the cell, where for large smoothing scales the distribution is Gaussian whereas, for small scales, the distribution is approximately log-normal. So for each cell size, one

should calculate the CIC distribution, which is a computationally expensive procedure. Finally, we conclude that although the CIC is a computationally costly process, it is advantageous to explore different regimes and compare the linear and non-linear scales.

Another quantity defined to study non-linear scales is the void probability (VP) function. It is defined as the probability of a volume (such as a sphere) to be empty. White (1979) derived the relation of the VP function with higher-order correlations and showed that the VP is a generating function for the CIC distribution. Moreover, a remarkable feature of the VP function is its scaling relation. It was shown that for some proposed phenomenological models of n -point correlation functions in a strongly non-linear regime, the VP function inherits a scaling relation. This relation has a universal behaviour as a function of scale (White 1979; Balian & Schaeffer 1989; Bernardeau 1992; Szapudi & Szalay 1993; Munshi et al. 1999). Investigating the galaxy surveys and numerical simulations data exhibit the existence of this universal behaviour for galaxy magnitude and halo mass respectively. (Fry 1986; Maurogordato & Lachieze-Rey 1987; Maurogordato & Lachieze-Rey 1991; Croton et al. 2004; Fry & Colombi 2013).

The VP function has been widely used in cosmological studies. Sharp (1981) used the VP function in large scales to study the n -point correlation function. Walsh & Tinker (2019) used it to study the galaxy assembly bias. Paranjape & Alam (2020) introduced the Voronoi volume function and its sensitivity to the cosmological parameters. Banerjee & Abel (2020, 2021) introduced a new probe named the k -nearest neighbour (k -NN) distance from a Poisson distributed random points, which improves the constraints on the cosmological parameters. In this work, we use the spherical contact cumulative/probability distribution function (SC-CDF/PDF) which is complementary to the VP function.

According to the definition of the VP function, it probes mainly the cosmic voids, and it is not sensitive to the details of the structures. Accordingly, changing the halo finder method does not have a significant impact on the VP function. The nearest neighbour cumulative/probability distribution function (NN-CDF/PDF), on the other hand, is a probe that is more sensitive to the details of the structures (Clark & Evans 1954; Soneira & Peebles 1977; Martinez & Saar 2001; Baddeley et al. 2006; Chiu et al. 2013). The NN-CDF is the complementary probability of finding an empty spherical region with a halo or galaxy at its centre. So it is more sensitive to clustering and entails different information compared to the VP function. In this direction, we also define a new quantity by combining the VP function and the NN-CDF, called the J-function (Van Lieshout & Baddeley 1996; Kerscher et al. 1999) (see theoretical background section).

The relation of the previously mentioned probes to the cosmological parameters and the initial conditions of the universe is not straightforward, and we often need to perform a numerical simulation to obtain them. However, we can use these probes to compare different samples. These samples are made by considering different redshift or mass/magnitude limit of halos/galaxies. Both possibilities when one compares different samples are interesting. If the functions are mass-scale/redshift independent, it leads us to define universal scales. If the functions evolve with redshift or/and are mass scale-dependent, it could be a sign of an interesting physics behind this evolution/dependence.

Finding the origin of the universality behaviour is crucial. It could be the result of gravitational instability and non-linear evolution or it could be a characteristic of the initial conditions. Whatever the answer is, we can check the universality in different theories (simulations) and observations.

Accordingly, we prepare different samples, by considering mass limit and different redshift snapshots in simulations. We explore numerical N-body simulations as well as the galaxy group catalogues. We calculate the SC-CDF, NN-CDF, and J-function. Moreover, we study the SC-PDF, NN-PDF and calculate their moments. We also introduce the logarithmic moments to distinguish different samples. In this work, we show that the SC-CDF and NN-CDF probe non-linear scales differently. We employ the N-body simulations in the redshift range of zero to unity with different mass limits ($10^{11} - 10^{14} M_{\odot} h$) to study the time evolution and mass dependence of the SC-CDF and NN-CDF.

The structure of this work is as follows: In Section 2, we review the theoretical background of the non-linear quantities, the SC-CDF, NN-CDF and J-function. In Section 3 we go through the numerical simulations data and calculate these measures for different samples. In Section 4 we show results for the galaxy groups and finally, in Section 5 we conclude and point out the future remarks.

2 THEORETICAL BACKGROUND

In this section, we use a class of summary statistics that encapsulate information from higher-order correlations in an optimum way. We consider the SC-CDF (which is equivalent to the VP function), NN-CDF, and J-function. There are three theoretical points of view to study these quantities; a) Their relation to n -point correlation function (see Subsection 2.1). b) The shape of their probability distributions. In this direction, we introduce the normal and log-normal distribution functions, which are relevant to the linear and non-linear statistics, respectively (see Subsection 2.2) and c) The scaling relations corresponding to these quantities (see Appendix A).

2.1 Relations to the n -point correlation functions

The frequently used statistical measure for point processes (Chiu et al. 2013) is the two-point correlation function $\xi_2(r)$,

$$\langle n(\mathbf{r}_1)n(\mathbf{r}_1 + \mathbf{r}) \rangle = [1 + \xi_2(r)]n^2, \quad (1)$$

where $n(\mathbf{r})$ is the number density of points and $n = \langle n(\mathbf{r}) \rangle$ is mean number density. In linear scales the density field is a Gaussian distribution and the two-point correlation $\xi_2(r)$ and n have all the field information. In non-linear scales due to the non-Gaussianity we have to consider other n -point correlations $\xi_n(\mathbf{r}_1, \dots, \mathbf{r}_n)$. White (1979) introduced conditional correlation functions (Ξ_i) as a connection between the VP and n -point correlation functions.

$$\Xi_i(\mathbf{r}_1, \dots, \mathbf{r}_i; V) = \sum_{j=0}^{\infty} \frac{(-n)^j}{j!} \int \dots \int \xi_{i+j}(\mathbf{r}_1, \dots, \mathbf{r}_{i+j}) dV_{i+1} \dots dV_{i+j}, \quad (2)$$

where the integrals are taken over the volume V and by definition $\xi_0 = 0$ and $\xi_1 = 1$. The ordinary correlation $\xi_n(\mathbf{r}_1, \dots, \mathbf{r}_n)$ corresponds to the probability that n -points defined in positions $\mathbf{r}_1, \mathbf{r}_2 \dots, \mathbf{r}_n$. Due to statistical homogeneity and isotropy, the correlations depend only on relative positions of the points. However, the conditional correlation have an additional property that the volume V to be empty. So it depends on the position of points in the volume V (White 1979).

The SC-CDF is the cumulative distribution of the distance between

randomly distributed positions in space and their nearest neighbour, taken from a sample. We show the SC-CDF by $F(r)$ where r is the relative distance between random positions and their nearest neighbour. In other words, $F(r)$ is the probability that the nearest neighbour distance of a random point in space to be equal or smaller than r . On the other hand, the NN-CDF is the cumulative distribution of the distance between a halo/galaxy and their nearest neighbour (which itself is a halo/galaxy), both from the same sample. We show this function by $G(r)$. Equivalently, the $G(r)$ is the probability that the nearest neighbour distance of a halo/galaxy to be equal or smaller than r .

The complementary cumulative distribution function related to the SC-CDF is equal to the probability that all sample points to be out of the sphere with volume V . So there is a direct relation between the SC-CDF and the VP function (the probably that a sphere to be empty),

$$P_0(V(r)) = 1 - F(r), \quad (3)$$

where P_0 is the VP function and $V(r) = \frac{4\pi}{3}r^3$. White (1979) calculated the relation between the VP function and the zero conditional correlation function

$$P_0(V) = \exp [\Xi_0(V(r))]. \quad (4)$$

Equations (2,4) show that all higher-order correlation functions influence the VP function and the SC-CDF. Accordingly the SC-CDF is

$$F(r) = 1 - \exp [\Xi_0(V(r))]. \quad (5)$$

The complementary cumulative distribution $1 - G(r)$, related to the NN-CDF $G(r)$ is the probability that a point to be in the centre of an empty sphere. Using the conditional correlations we have

$$G(r) = 1 - \Xi_1(\mathbf{r}_o; V(r)) \exp [\Xi_0(V(r))], \quad (6)$$

where \mathbf{r}_o is the position vector of the sphere's centre, which can be set to zero by a coordinate transformation. $\Xi_1(\mathbf{r}_o, V(r))$ is the conditional probability of a point in the centre of an empty volume V and $\exp [\Xi_0(V(r))]$ is the probability of the void function. Comparing the SC-CDF with the NN-CDF, we should note that the former depends only on the zeroth-order conditional correlation. However, the latter is related to the first conditional probability. It is important to notice that the NN-CDF is more sensitive to clustering compared to the SC-CDF. As voids occupy the larger portions of the cosmic web, the SC-CDF (which is the probability of a region to be empty) explores the larger scales. In contrast, the NN-CDF is useful to study the high-density regions and, accordingly, the smaller scales. Now, we can define the J-function as

$$J(r) = \frac{1 - G(r)}{1 - F(r)} = \Xi_1(\mathbf{r}_o; V(r)), \quad (7)$$

which only has $\Xi_1(\mathbf{r}_o; V(r))$ dependency. If the data is Poisson random set with zero correlation between points, then we have

$$F(r) = G(r) = 1 - \exp \left(-\frac{4\pi}{3}nr^3 \right). \quad (8)$$

Thus for a sample without any correlation, we have $J = 1$. Accordingly, the J-function is a better measure of clustering compared to the SC-CDF and NN-CDF. The J-function for the samples with positive correlation is below unity $J < 1$, and for anti-correlated ones, we have $J > 1$, which is helpful to distinguish these two types as well (Kerscher et al. 1999).

Moreover, we can find a relation for the probability distribution functions by taking the derivative of equation (5) and equation (6)

with respect to r . For this task, first we have to calculate the derivative of the conditional correlations, equation (2) with respect to the variable r , radius of the sphere V . Due to spherical symmetry, we have

$$\frac{d}{dr} \Xi_0(V(r)) = (-4\pi r^2 n) \Xi_1(\mathbf{r}_s; V(r)), \quad (9)$$

where \mathbf{r}_s is a vector on the boundary of sphere and $\Xi_1(\mathbf{r}_s; V(r))$ is only a function of $|\mathbf{r}_s| = r$. Using equations (5,9), we have

$$\left| \frac{dF(r)}{dr} \right| = 4\pi r^2 n \Xi_1(\mathbf{r}_s; V) \exp[\Xi_0(V)]. \quad (10)$$

To calculate the NN-PDF we must know the derivative of the first conditional correlation at position \mathbf{r}_o . Again due to spherical symmetry we can calculate the derivatives analytically. From equation (2) we find that

$$\frac{d}{dr} \Xi_1(\mathbf{r}_o; V(r)) = (-4\pi r^2 n) \Xi_2(\mathbf{r}_s, \mathbf{r}_o; V(r)), \quad (11)$$

where \mathbf{r}_o is the centre of the sphere, where we can set $\mathbf{r}_o = 0$ by a coordinate transformation. So $\Xi_2(\mathbf{r}_s, \mathbf{r}_o; V(r))$ is symmetric and only a function r . Finally, we have

$$\left| \frac{dG(r)}{dr} \right| = 4\pi r^2 n [\Xi_1(\mathbf{r}_s; V) \Xi_1(\mathbf{r}_o; V) + \Xi_2(\mathbf{r}_s, \mathbf{r}_o; V)] \exp[\Xi_0(V)], \quad (12)$$

where again \mathbf{r}_s is a vector on the sphere's boundary. By comparing the SC-PDF and the NN-PDF from equations (10,12), we find that the NN-PDF is related to the higher-order conditional probabilities in contrast to the SC-PDF. We also can compare the SC-PDF with the NN-CDF from equation (6). The two equations have similarities when both depend on Ξ_1 . However, the SC-PDF is the probability that depends on \mathbf{r}_s , while the NN-CDF depends on \mathbf{r}_o .

One way to calculate the SC-CDF for a data set is to draw spheres with radius r in space randomly. To find the SC-CDF we calculate the ratio of the empty to total spheres as

$$1 - F(r) = \frac{N_{\text{empty}}}{N_{\text{total}}}. \quad (13)$$

This approach works for the NN-CDF too. We set the centre of all spheres on the sample points and repeat the procedure in different r . The efficient approach to calculate the SC-CDF/SC-PDF is to create a randomly distributed Poisson sample. We calculate the distance between random points to their nearest neighbour chosen from observation/simulation data points. We can directly calculate the probability and cumulative distributions with ordered distances. For the NN-CDF/NN-PDF the procedure is similar, but we choose all the points from observation/simulation data. For the SC-CDF the number of Poisson sample points is arbitrary. We calculate the SC-CDF/SC-PDF with the same number of random points as the observation/simulation data. We follow this procedure to have a better comparison with NN-CDF/NN-PDF. Accordingly, we obtain the J -function consistently (for another choice of random point's number, see Banerjee & Abel (2020)). Hereafter, we calculate the aforementioned functions with respect to a new introduced dimensionless variable x defined as

$$x = \left(\frac{4\pi}{3} n \right)^{1/3} r. \quad (14)$$

The privilege of using the dimensionless variable x is that we omit the effect of the mean number density. Accordingly, the SC-NN functions depend only on the n -point correlation functions. Further, we can use x in the conditional correlations as well, equation (2), to remove the effect of number density. For more details see, Appendix (A).

2.2 Probability distributions

The normal (Gaussian) probability distribution function $\mathcal{N}(\mu, \sigma)$ is defined as follows,

$$f_n(x) = \frac{1}{\sqrt{2\pi}\sigma} \exp[-(x - \mu)/2\sigma^2]. \quad (15)$$

In linear scales, the matter distribution is normal as a result of the single field inflationary models. In non-linear scales the matter distribution is nearly log-normal distribution as below

$$f_l(y) = \frac{1}{\sqrt{2\pi}y\sigma} \exp[-(\log(y) - \mu)/2\sigma^2]. \quad (16)$$

where the above equation is obtained by changing variable $y \equiv e^x$ in a normal distribution, Equation (15). The difference between the normal and log-normal distribution from the central limit theorem point of view is discussed in Coles & Jones (1991), as well. The theorem works for a stochastic variable, which is a sum over other variables $X = \sum_{i=1}^N X_i$. For large N statistics the distribution tends to be normal $f(x) \rightarrow \mathcal{N}(\mu, \sigma)$. In our context, in linear scales, the matter density contrast is a sum over independent modes of Fourier space, consequently its statistics is Gaussian. For non-linear quantities where $Y = \prod_{i=1}^N X_i$ and for large number N , the logarithm of Y can be written as $\log(Y) = \sum_{i=1}^N \log(X_i)$. So the central limit theorem implies a normal distribution, equation (16), for $\log(Y)$ and log-normal distribution for Y . In standard perturbation theory as a result of mode coupling the non-linear density contrast is constructed by multiplication of linear density contrast with corresponding kernels (Bernardeau et al. 2002) and as a result we expect an approximately log-normal distribution for matter density in non-linear scales.

In the next section, we calculate the moments of the SC-PDF, where the skewness is not small. We introduce the skew normal distribution as

$$f_s(x) = f_n(x)[1 + \text{erf}(\alpha \bar{x})], \quad (17)$$

where $f_n(x)$ is the normal distribution (equation (15)), α is a constant, $\bar{x} = \frac{x - \mu}{\sqrt{2}\sigma}$ and erf is the error function,

$$\text{erf}(x) = \frac{2}{\sqrt{\pi}} \int_0^x e^{-t^2} dt. \quad (18)$$

In this work, we fit the SC-PDF and NN-PDF with the mentioned distributions and discuss the probable deviations. We can also characterise the distribution functions by their moments. The n th moment of a distribution function $f(x)$ is defined as,

$$s_n = \int (x - \mu)^n f(x) dx, \quad (19)$$

in which μ is the mean of distribution. Zero moment is unity $s_0 = 1$ for a normalised distribution and we have $s_1 = 0$ by definition. We define the skewness and kurtosis by $\tilde{s}_3 = s_3/s_2^{3/2}$ and $\tilde{s}_4 = s_4/s_2^2$, respectively. For a normal distribution equation (15), variance $s_2 = \sigma^2$, skewness is $\tilde{s}_3 = 0$ and kurtosis is $\tilde{s}_4 = 3$. We extend this concept to the logarithmic case and introduce the corresponding moments as

$$l_n = \int (\ln(x) - \mu)^n f(x) dx, \quad (20)$$

where μ is the logarithmic mean of distribution. Note that by definition $l_0 = 1$ and $l_1 = 0$ is for a normalised distribution. For a log-normal distribution equation (16), we can calculate higher moments $l_2 = \sigma$, $l_3 = 0$, and $l_4 = 3\sigma^2$. Accordingly, the logarithmic skewness and kurtosis of a log-normal distribution are $\tilde{l}_3 = l_3/l_2^{3/2} = 0$,

Table 1. We present the details of the different dark matter halo samples from the SMDPL simulation. The conditions on mass and redshift are shown in columns 1 and 2, respectively. And $r_\star = r/(nV)^{1/3}$ is represented in column 3.

$\log(M_{\text{lim}}/M_\odot h)$	redshift(z)	r_\star (Mpc/h)
11	0	1.963
11	0.5	1.942
11	1	1.943
11.5	0	2.759
11.5	0.5	2.758
11.5	1	2.803
12	0	3.884
12	0.5	3.949
12	1	4.114
12.5	0	5.53
12.5	0.5	5.76
12.5	1	6.234
13	0	8.019
13	0.5	8.689
13	1	9.981
13.5	0	12.083
13.5	0.5	13.953
13.5	1	17.624
14	0	19.781
14	0.5	25.163
14	1	36.904

and $\tilde{l}_4 = l_4/l_2^2 = 3$. The logarithmic moments are especially useful when we study the distributions in non-linear scales.

The normal and log-normal moments naturally define two classes of distributions. As a specific indicator, if the kurtosis of distribution is $\tilde{s}_4 \sim 3$, the distribution is nearly linear or normal and if the logarithmic distribution has a kurtosis $\tilde{l}_4 \sim 3$ the distribution is nearly non-linear or log-normal. In the next section, we will show that the SC-PDF is linear and, the NN-PDF is a non-linear distribution.

3 SIMULATIONS

As we discussed, it is intricate to calculate the NN-CDF/PDF, SC-CDF/PDF, and J-functions by analytical prescription of Section 2. Accordingly, we explore these functions in cosmological simulations. In the first subsection, we explain the simulations and methods we used in this work, and we will present the results in the second subsection.

3.1 SMDPL simulation

In this work, we use the simulations publicly available in the "MultiDark" project (Riebe et al. 2013). The project includes several simulations with different box sizes, seed numbers, and different number of particles¹. As we are interested in non-linear scales, roughly below 10 Mpc, the resolution should be high enough to capture the relevant scales. To have a statistically enough number of

halos, we need a large box size to probe the end tails of the distributions. To satisfy these two conditions together, we choose the Small MultiDark Planck (SMDPL) simulation. The SMDPL box size is 400Mpc/h and it has 3840^3 particles. The cosmological parameters are as Planck 2014 (Ade et al. 2014), $h = 0.6777$, $\Omega_\Lambda = 0.692885$, $\Omega_m = 0.307115$, $\Omega_b = 0.048206$, $n_s = 0.96$ and $\sigma_8 = 0.8228$. Three redshifts $z = 0$, $z = 0.49$ ², and $z = 1$ are considered in simulations to explore the redshift evolution of the quantities. For each redshift, we create different samples by limiting the mass of halos to find the scale dependence of the quantities. Accordingly, we choose 7 different mass limits $\log(M/M_\odot h) > \{11.5, 12, 12.5, 13, 13.5, 14\}$. In total, we have $3 \times 7 = 21$ different samples, which we use to calculate the mass and redshift dependence of these quantities (i.e., the SC-CDF, NN-CDF, and J-function). In Table (1) we summarize the characteristics of the different samples, and report the $r_\star = 1/\sqrt[3]{(4\pi n/3)}$ for each sample. Note that throughout this paper, all the statistical quantities including moments are expressed with the dimensionless variable $x = r/r_\star$ in which r is the physical comoving length (Section 2). We explore the results from the two other simulations of the MultiDark project to check the consistency and robustness of the result concerning simulation characteristics in Appendix (B).

The statistical quantities we introduced in the previous section could be computed using dark matter halos or particles in N -body simulations. In this work, we use the position of dark matter halos to measure these quantities. We use dark matter halos provided by Riebe et al. (2013). These halos have been identified using the FoF method (Lacey & Cole (1994)) and the linking-length is set to $b = 0.2$. As we have the positions and properties of the dark matter halos, we can calculate the SC-CDF, NN-CDF, and J-function for these halos directly using the methods introduced in Section 2. We calculate the statistical errors by dividing the simulation box into 27 similar sub-boxes, and use them as sub-samples with the assumption of the statistical homogeneity. We calculate the quantities in each sub-sample, and we report the mean and standard deviation of these sub-boxes with corresponding conservative error bars. For more details see Appendix B. We also follow a similar approach to find errors in observational data in Section 4.

3.2 Results

We discuss the mass scale and redshift dependence of the SC-CDF/PDF, NN-CDF/PDF, and J-function using cosmological N -body simulations. Specifically, in this subsection, we represent results obtained from the dark matter halos of the SMDPL simulation. To see the general behaviour of the SC-PDF and NN-PDF in Fig. 1, we plot the SC-PDF (thick solid red line) and the NN-PDF (thin solid red line) of dark matter halos as a function of $x = \sqrt[3]{nV}$. In Fig. 1, the redshift is $z = 0$ and the mass limit is set to $M > 10^{11} M_\odot$. It is clear that both the SC-PDF and NN-PDF have visible peaks around $x \sim 0.5$ and $x \sim 1.2$ and these numbers can be translated to a physical comoving length of $r = r_\star x \approx 1$ Mpc/h and $r \approx 2.3$ Mpc/h respectively. Note that for this specific sample $r_\star = 1.963$ (see Table (1)). Based on Fig. 1, the SC-PDF approximately follows skew-normal, equation (17), with parameters $\mu = 0.55$, $\sigma = 1$, $\alpha = 2.6$ (dashed thick blue line), and the NN-PDF approximately is log-normal, equation (16), with parameters $\mu = -0.75$, $\sigma = 0.55$ (dotted-dashed thin blue line). Here, we have the idea of using the normal and log-normal distributions as the anchor of our study for linear and non-linear scales. It is

¹ Find the complementary information of these simulations in the web page <https://www.cosmosim.org>

² In figures and, tables we show it with one digit accuracy $z = 0.5$

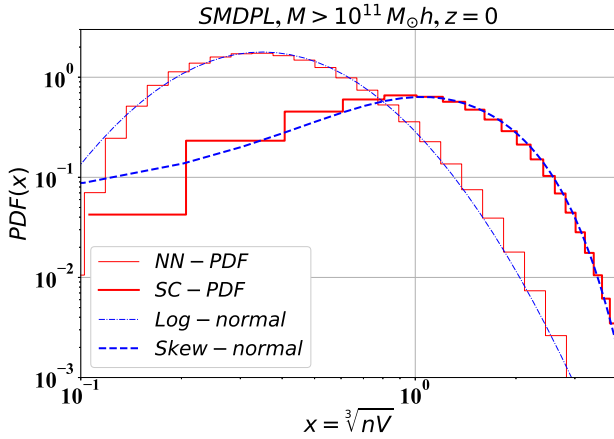


Figure 1. The NN-PDF and SC-PDF for dark matter halos are plotted as a function of the dimensionless variable x for the SMDPL simulation. In this figure, we set the mass limit to $M > 10^{11} M_{\odot} h$ and the redshift is $z = 0$. Thin red line refers to the NN-PDF and the thick red line refers to the SC-PDF. Dot-dashed thin blue line is the theoretical log-normal curve equation (16) with $\mu = -0.75$, $\sigma = 0.55$. The dashed thick blue line is the skew-normal curve equation (17) with $\mu = 0.55$, $\sigma = 1$, $\alpha = 2.6$.

worth mentioning that the theoretical curves are not precise, and the simulation data deviates from these curves, especially at the tail of the distributions. For example the distance variable x , in equation (14), is always positive, while our fitting (normal and the skew-normal) distributions would give non-zero (although small) values for negative x which is not physical. This issue also exists when considering the matter density field as a normal distribution Gaztanaga et al. (2000). However, the log-normal distribution seems to be more appropriate to address this issue when we use positive variables. Testing the robustness of more complex distributions (for example, the Edgeworth expansion) will be the subject of our future works. (Gaztanaga et al. 2000; Shin et al. 2017) Considering the general behaviour of the distributions, the SC-PDF is nearly skew-normal, and the NN-PDF is nearly log-normal. The SC-PDF is defined based on the distance between one halo to a random point in a sample, while the NN-PDF is defined according to the position between two halos. As we mentioned previously, due to the central limit theorem, the SC-PDF is a linear distribution (it is related to the general shape of the cosmic web) and the NN-PDF is a non-linear distribution (it depends on details of the structures' distribution).

We make four samples from Table (1). This is done by applying conditions on mass scale, $\log(M/M_{\odot} h) > \{11, 13\}$, and redshift $z = \{0, 1\}$. In Fig. 2, we present a) the SC-CDF, b) the NN-CDF, and c) the J-function in terms of $x = \sqrt[3]{nV}$. The red circles represent $z = 0$ with lower mass limit of $10^{11} M_{\odot} h$, the blue squares correspond to $z = 1$ with lower mass limit of $10^{11} M_{\odot} h$, green up-pointing triangles correspond to $z = 0$ with lower mass limit of $10^{13} M_{\odot} h$ and black down-pointing triangles correspond to $z = 1$ with lower mass limit of $10^{13} M_{\odot} h$.

According to part (a) of Fig. 2, the SC-CDF is redshift-independent while it shows a mass-limit dependence in the range of $x > 1$. (Banerjee & Abel 2020) asserts that when we study tail of the distributions with a new quantity, namely "peaked CDF", we can distinguish the SC-CDF in two different redshift samples. In panel (b) of Fig. 2, the difference between distinct mass scales is clear (similar to the panel a). Moreover, the NN-CDF has a clear redshift

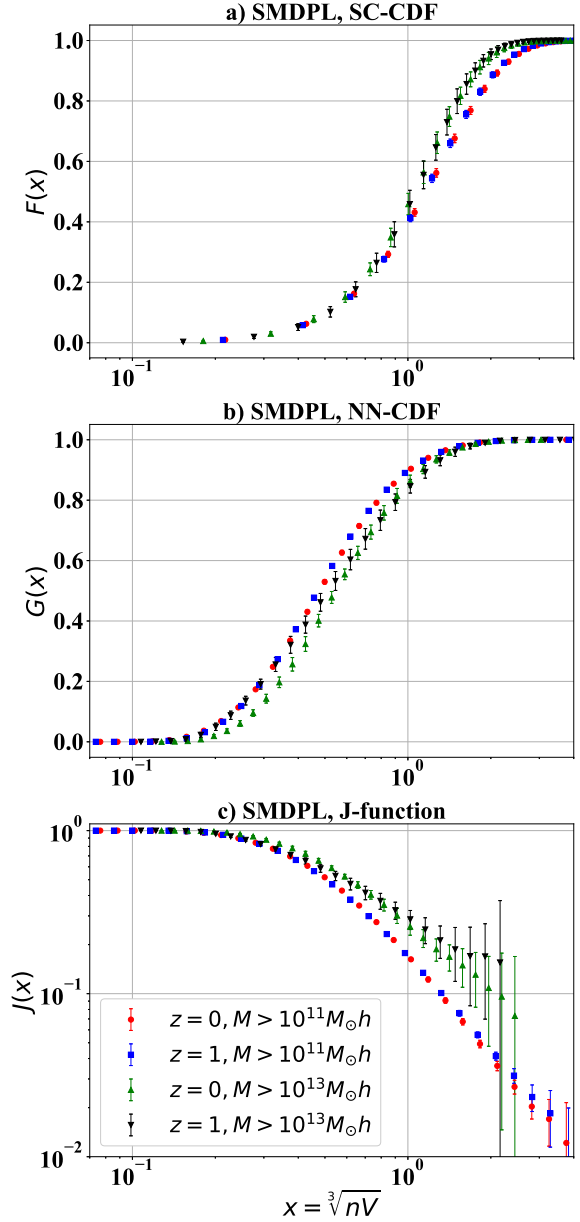


Figure 2. In this figure, a) $F(x)$, the SC-CDF, b) $G(x)$, the NN-CDF and c) $J(x) = \frac{1 - G(x)}{1 - F(x)}$ as a function of $x = \sqrt[3]{nV}$ are plotted using halos from the SMDPL simulation. The red circles ($z = 0$) and the blue squares ($z = 1$) correspond to lower mass limit of $10^{11} M_{\odot} h$ and green up-pointing triangles ($z = 0$) and black down-pointing triangles ($z = 1$) correspond to lower mass limit of $10^{13} M_{\odot} h$.

evolution in the redshift range of zero to unity for the lower mass limit of $10^{13} M_{\odot} h$. Based on the curves in Fig. 2 the SC-CDF is a better function to find the similarities, while the NN-CDF helps to distinguish different samples. In panel (c) of Fig. 2 we plot the J-function. The J-function is sensitive to the clustering, so we see that in the lower mass ranges, the halos are more clustered in the deep non-linear regime.

To study the similarities and differences of the samples more precisely, we calculate the moments of the SC-PDF and report it in Table (2). In Table (3), we calculate the logarithmic moments of the NN-PDF. In general, calculating the moments helps us to sum-

Table 2. The moments of the SC-PDF for the samples of Table (1) calculated using equation (19). The condition on the mass and redshift are presented in column 1 and 2 respectively. s_1 , s_2 , \tilde{s}_3 and \tilde{s}_4 are reported in the next columns, respectively.

$\log(M_{\text{lim}}/M_{\odot}h)$	redshift(z)	s_1	s_2	\tilde{s}_3	\tilde{s}_4
11	0	1.265 ± 0.025	0.647 ± 0.017	0.845 ± 0.047	3.827 ± 0.192
11	0.5	1.251 ± 0.024	0.633 ± 0.016	0.83 ± 0.045	3.819 ± 0.193
11	1	1.244 ± 0.024	0.624 ± 0.016	0.798 ± 0.043	3.711 ± 0.177
11.5	0	1.215 ± 0.027	0.601 ± 0.019	0.78 ± 0.055	3.677 ± 0.208
11.5	0.5	1.206 ± 0.028	0.591 ± 0.018	0.758 ± 0.049	3.622 ± 0.210
11.5	1	1.204 ± 0.027	0.585 ± 0.016	0.737 ± 0.051	3.584 ± 0.183
12	0	1.172 ± 0.032	0.563 ± 0.022	0.713 ± 0.082	3.520 ± 0.304
12	0.5	1.168 ± 0.03	0.554 ± 0.019	0.685 ± 0.052	3.441 ± 0.202
12	1	1.166 ± 0.03	0.545 ± 0.017	0.647 ± 0.051	3.353 ± 0.182
12.5	0	1.136 ± 0.037	0.53 ± 0.024	0.667 ± 0.097	3.456 ± 0.357
12.5	0.5	1.133 ± 0.035	0.522 ± 0.027	0.636 ± 0.141	3.419 ± 0.538
12.5	1	1.133 ± 0.042	0.515 ± 0.030	0.603 ± 0.158	3.373 ± 0.597
13	0	1.111 ± 0.048	0.504 ± 0.038	0.638 ± 0.235	3.508 ± 0.805
13	0.5	1.104 ± 0.044	0.491 ± 0.033	0.614 ± 0.181	3.46 ± 0.724
13	1	1.111 ± 0.053	0.483 ± 0.032	0.511 ± 0.168	3.173 ± 0.505
13.5	0	1.087 ± 0.062	0.475 ± 0.039	0.545 ± 0.182	3.150 ± 0.560
13.5	0.5	1.066 ± 0.057	0.455 ± 0.050	0.436 ± 0.204	2.992 ± 0.569
13.5	1	1.053 ± 0.076	0.438 ± 0.046	0.495 ± 0.315	3.172 ± 1.135
14	0	1.025 ± 0.071	0.427 ± 0.06	0.38 ± 0.419	2.987 ± 1.317
14	0.5	1.032 ± 0.092	0.412 ± 0.073	0.236 ± 0.344	2.562 ± 0.516
14	1	0.960 ± 0.130	0.353 ± 0.116	0.248 ± 0.499	2.444 ± 0.613

Table 3. The logarithmic moments of the NN-PDF for the samples of Table (1) calculated by equation (19). The condition and limit on mass and redshift are presented in column 1 and 2 respectively. l_1 , l_2 , \tilde{l}_3 and \tilde{l}_4 are in following columns, respectively.

$\log(M_{\text{lim}}/M_{\odot}h)$	redshift(z)	l_1	l_2	\tilde{l}_3	\tilde{l}_4
11	0	-0.728 ± 0.01	0.561 ± 0.005	0.12 ± 0.011	2.706 ± 0.015
11	0.5	-0.725 ± 0.009	0.553 ± 0.004	0.157 ± 0.01	2.708 ± 0.015
11	1	-0.731 ± 0.009	0.553 ± 0.004	0.199 ± 0.01	2.711 ± 0.014
11.5	0	-0.687 ± 0.010	0.549 ± 0.006	0.099 ± 0.015	2.679 ± 0.023
11.5	0.5	-0.687 ± 0.010	0.543 ± 0.005	0.146 ± 0.016	2.688 ± 0.018
11.5	1	-0.699 ± 0.010	0.546 ± 0.006	0.193 ± 0.021	2.670 ± 0.024
12	0	-0.649 ± 0.010	0.538 ± 0.007	0.076 ± 0.027	2.637 ± 0.035
12	0.5	-0.655 ± 0.010	0.535 ± 0.007	0.139 ± 0.025	2.641 ± 0.038
12	1	-0.677 ± 0.013	0.546 ± 0.009	0.191 ± 0.028	2.586 ± 0.043
12.5	0	-0.618 ± 0.016	0.53 ± 0.012	0.081 ± 0.041	2.606 ± 0.062
12.5	0.5	-0.629 ± 0.016	0.536 ± 0.012	0.151 ± 0.047	2.565 ± 0.074
12.5	1	-0.664 ± 0.022	0.561 ± 0.011	0.167 ± 0.056	2.477 ± 0.065
13	0	-0.591 ± 0.028	0.531 ± 0.018	0.102 ± 0.045	2.548 ± 0.108
13	0.5	-0.604 ± 0.032	0.551 ± 0.017	0.140 ± 0.077	2.463 ± 0.097
13	1	-0.651 ± 0.042	0.600 ± 0.020	0.078 ± 0.085	2.292 ± 0.110
13.5	0	-0.563 ± 0.049	0.547 ± 0.023	0.064 ± 0.125	2.445 ± 0.211
13.5	0.5	-0.591 ± 0.077	0.580 ± 0.029	-0.004 ± 0.137	2.309 ± 0.190
13.5	1	-0.619 ± 0.091	0.656 ± 0.046	-0.105 ± 0.242	2.250 ± 0.236
14	0	-0.508 ± 0.074	0.563 ± 0.050	-0.032 ± 0.237	2.330 ± 0.348
14	0.5	-0.529 ± 0.131	0.641 ± 0.082	-0.263 ± 0.277	2.320 ± 0.457
14	1	-0.511 ± 0.270	0.699 ± 0.228	-0.241 ± 0.533	1.932 ± 0.497

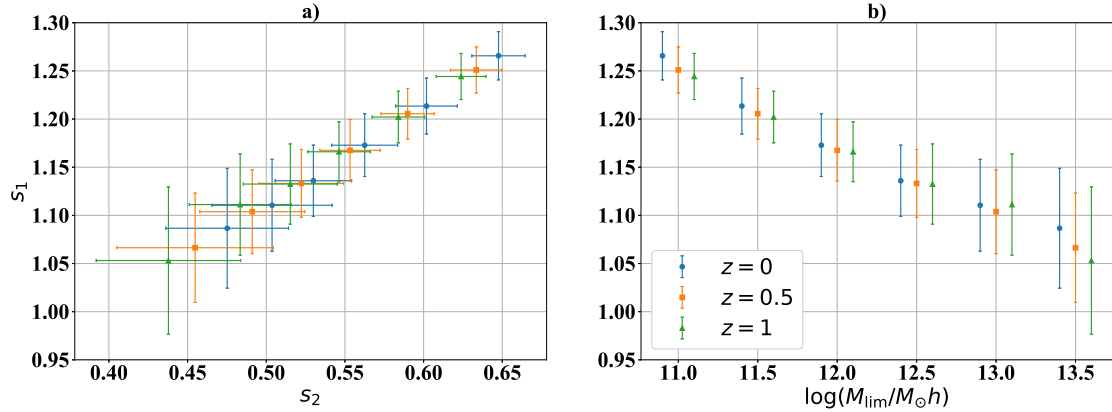


Figure 3. The first moment of the SC-PDF for dark matter halos of the SMDPL samples, s_1 defined in equation (19), is plotted for different mass scales with respect to a) s_2 and b) mass limits. Blue circles correspond to $z = 0$, orange squares are for $z = 0.5$, and green triangles are for $z = 1$. In panel (b), the mass scales are shifted slightly for clarification.

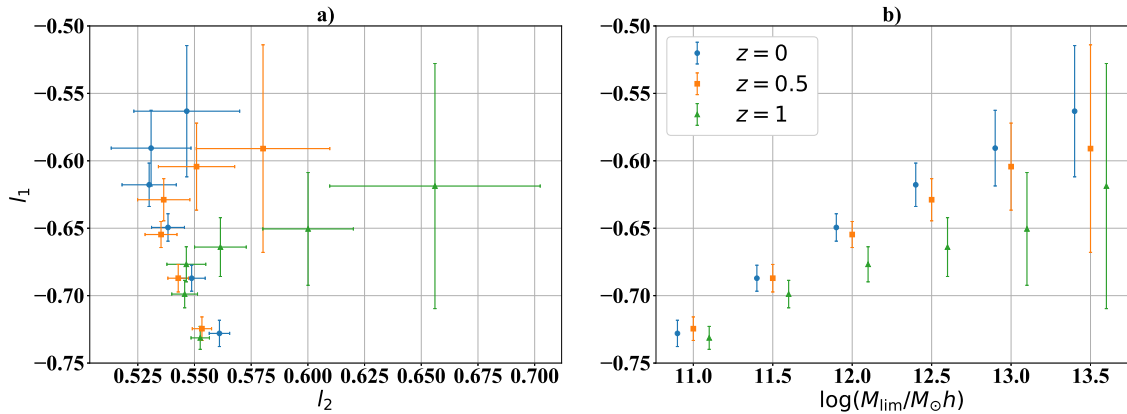


Figure 4. The first logarithmic moment of the NN-PDF for dark matter halos of the SMDPL samples, l_1 defined in equation (20), is plotted versus a) l_2 and b) mass limits for different mass scales. The labels are the same as Fig.3. In panel (b), the mass scales shifted slightly for clarification.

marise the information about the distributions of samples. The first and second columns of Table (2) show conditions on mass scale and redshift and the other four columns are s_1 , s_2 , \tilde{s}_3 and \tilde{s}_4 respectively (l_1 , l_2 , \tilde{l}_3 and \tilde{l}_4 for NN-PDF in Table (3)). Note that in Table (2) kurtosis, \tilde{s}_4 , of the SC-PDF varies from (3.8 ± 0.2) for mass scale 10^{11} to (3 ± 1) for mass scale 10^{14} . This again indicates that we can interpret the SC-PDF as a nearly normal distribution. The situation is different for the NN-PDF when logarithmic kurtosis \tilde{l}_4 is approximately 3. According to Table (3) \tilde{l}_4 varies from (2.7 ± 0.02) for mass scale 10^{11} to (2.3 ± 0.3) for mass scale 10^{14} . In Appendix (C) we study general behaviour of the SC-PDF and the NN-PDF in more details. For the normal distribution, the skewness is zero, so the non-zero skewness shows the deviation from a normal distribution. Comparing Tables (2,3), columns 5, the SC-PDF is more skewed than the NN-PDF. For the SC-PDF, the skewness is between 0.2 and 0.8, and the skewness is above 0.5, except the mass limit $M > 10^{14} M_\odot h$. However, for the NN-PDF, the skewness is between -0.2 to 0.1 . Accordingly, we conclude that it is plausible to fit the SC-PDF with the skew-normal distribution.

In Fig. 3 and Fig. 4 we report the first and second moments of the

distributions. In Fig. 3, we plot the mean of the SC-PDF, s_1 , with respect to a) s_2 and b) mass limit ($\log(M/M_\odot)$). In Fig. 4, we show the logarithmic mean of the NN-PDF, l_1 , with respect to a) l_2 and b) mass limit ($\log(M/M_\odot h)$). In both figures, with respect to a) and b) mass limit ($\log(M/M_\odot h)$). In both figures, the blue circles represent redshift zero, the orange squares correspond to redshift 0.5, and the green triangles show redshift 1. For the sake of clarity in presentation, in panel(b) of the figures, the mass scales are shifted slightly with respect to each other for the redshifts samples. There is a one to one correspondence between the panels (a) and (b). In panel (a), the mass limits can be derived using panel (b). In Fig. 3, we study the different sample's similarities or differences. The SC-PDF s_1 and s_2 are similar for the different redshift samples with a fixed mass scale. Note that s_2 reveals the difference better than s_1 . For the NN-PDF, based on Fig. 4, for the low mass scales, l_1 versus l_2 is almost the same, while for larger masses, we have more scatters. l_2 is a better probe to distinguish the samples, while l_1 is almost constant over a specific mass-scale. Note that in the corresponding figures, higher mass scales have larger error bars which is due to small number of massive halos in N -body simulation data-sets.

In Fig. 3 panel (a) there is a positive correlation between s_1 and

Table 4. Different volume-limited catalogues are represented. The conditions on magnitude and redshift are presented in column one and two, respectively. $r_\star = r/(nV)^{1/3}$ is shown in column three. We report the number of groups in column four.

$M_{r,\text{lim}}$	z_{lim}	r_\star (Mpc/h)	N
-18	0.045	3.891	5258
-18.5	0.057	4.256	7761
-19	0.071	4.698	11352
-19.5	0.089	5.116	16517
-20	0.110	6.225	17301
-20.5	0.136	7.788	16444

s_2 which can be approximated by a linear relation. Accordingly, for each specific redshift, a linear function can be fitted as a proxy for comparing different cosmological models. The relation between l_1 and l_2 is more complicated for the NN-PDF which is shown in Fig. 4 panel (a). For the lower mass scales $\{11, 11.5\}$, l_1 and l_2 are anti correlated, while for the higher mass scales $\{12.5, 13, 13.5\}$ they become correlated. The mass scale 10^{12} is the turning point according to this plot. In summary, in this section we showed results for the SC-CDF/PDF, NN-CDF/PDF, and J-function in terms of the dimensionless variable x . We can mention our results in three conclusive points:

- 1) Similarity argument:** We find that for a specific mass scale, the first moment of the SC-CDF is almost independent of redshift till $z = 1$.
- 2) Distribution argument:** Exploring the general behaviour of distributions, the SC-PDF is nearly skew-normal, while the NN-PDF is nearly log-normal.
- 3) Moments dependency:** There is an approximately linear relation between the first and second moments, however for the NN-CDF, we have a bi-modal behaviour in the moments. In the next section, we continue our discussion using the observational data.

4 OBSERVATIONS

In this section, we study the SC-CDF/PDF, NN-CDF/PDF, and J-function for the galaxy group catalogues. Here, we are going to find the capability of the new probes to study clustering of galaxy groups. Galaxy groups are the luminous tracers of large mass dark matter halos. Accordingly, we can compare the results with N-body simulations. However, the exact comparisons need a more sophisticated approach to consider all the complication raised from the redshift space distortion, baryonic effects, and dark matter-luminous matter bias.

4.1 Sample selection

In this work, we use the galaxy group catalogues of Tempel et al. (2014). They provide flux-limited and volume-limited ones from SDSS-DR10 (York et al. (2000); Ahn et al. (2014)) data, and the upper limit on redshift is considered $z=0.2$. Tempel et al. (2014) used a modified version of FoF to find the galaxy groups, in which the linking-length is redshift dependent. The linking-length is defined as the average over the NN-PDF of the galaxies in a sample. The idea behind this choice is to make sure that the galaxies find the nearest neighbour in their group, and isolated galaxies that are in the tail of the distribution, do not change the mean of the NN-PDF (and linking length) significantly. Accordingly,

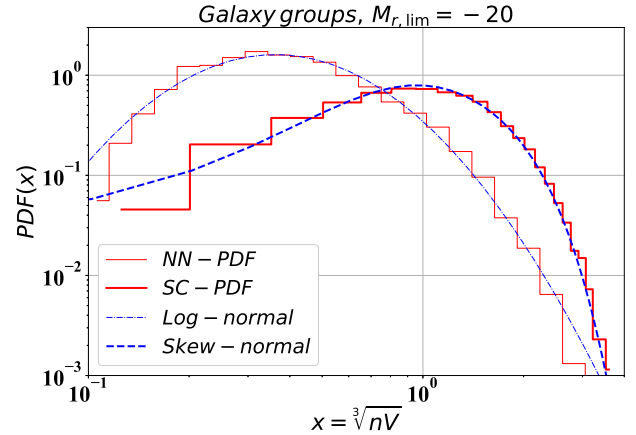


Figure 5. The NN-PDF and the SC-PDF for galaxy groups are plotted versus the dimensionless variable x for a volume limited catalogue. The condition on magnitude is $M_{r,\text{lim}} = -20$. Thin red line refers to NN-PDF and the thick red line refers to SC-PDF. Dot-dashed thin blue line is the theoretical log-normal curve equation (16) with $\mu = -0.68$, $\sigma = 0.58$ and dashed thick blue line is skew-normal curve equation (17) with $\mu = 0.56$, $\sigma = 0.8$, $\alpha = 2.6$.

the average over the NN-PDF is a reasonable estimation for the distances between galaxies in a group. It is interesting to note that, for the volume-limited catalogues, the linking-length is approximately constant over redshift.

In this work, we use 6 volume-limited catalogues from Tempel et al. (2014). The details of the catalogues are shown in Table (1). In the first column, we show the limit on the magnitude $M_{r,\text{lim}}$ and in the column 2, we report the limit on redshift. In Table (1) the column three is r_\star for each catalogue in unit of Mpc/h.

In order to find the physical distances to the galaxy groups we need to assume a background cosmology. We set the cosmological parameters similar to Section 3, in agreement with Planck (Ade et al. 2014).

To avoid boundary problems in sample selection, we use an area of $0 < \text{Dec} < 55$, $130 < \text{Ra} < 240$. In Table (1), column four, we report the number of groups for each volume-limited catalogues, after selection. To estimate the errors, we use a conservative approach similar to Section 3 and divide the sample into four equivalent sub-samples and calculate the mean and standard deviation of each sub-samples.

4.2 Results

In Fig. 5, we plot the SC-PDF (thick red line) and the NN-PDF (thin red line) for $M_{r,\text{lim}} = -20$ as a function of x . The SC-PDF peak is around 1.2, and the NN-PDF peak is at 0.5. They correspond to physical comoving lengths of 7.5 Mpc/h and 3.1 Mpc/h, respectively. Comparing the galaxy groups with simulations is challenging because of the differences between statistics of DM halos and galaxy groups. However, the general behaviour of dark matter distributions in N-body simulations (see Section 3) can be used as a hint for galaxy distributions. For example, we showed in Fig. 1 that the SC-PDF is nearly skew-normal, and the NN-PDF approximately follows a log-normal distribution for dark matter halos. This approximation seems viable for galaxy groups as well. In Fig. 5 dashed blue thick line, shows skew-normal

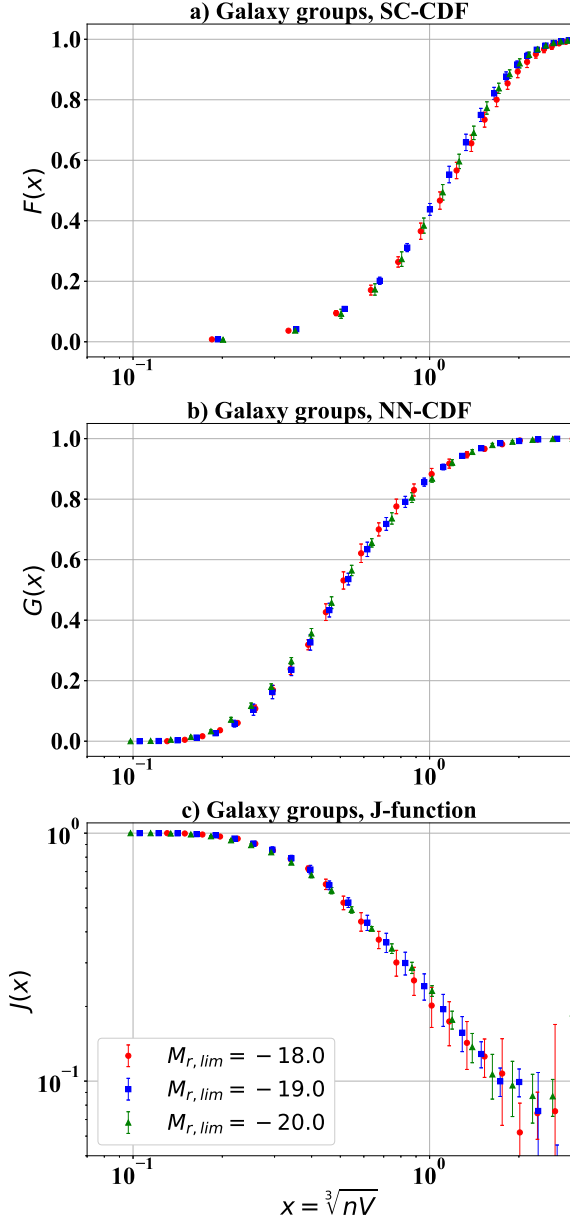


Figure 6. In this figure, in panels a) $F(x)$, SC-CDF, b) $G(x)$, NN-CDF and c) $J(x) = \frac{1 - G(x)}{1 - F(x)}$ versus $x = \sqrt[3]{nV}$ are plotted for galaxy groups of the volume limited catalogue. Red circles represent $M_{r,\text{lim}} = -18$, blue squares represent $M_{r,\text{lim}} = -19$, green triangles show $M_{r,\text{lim}} = -20$.

probability distribution function (equation (17)) with parameters $\mu = 0.56, \sigma = 0.8, \alpha = 2.6$ and dot-dashed blue thin line is a log-normal probability distribution function (equation (16)) with parameters $\mu = -0.68, \sigma = 0.58$. Here, similar to Section 3, we find the parameters when the distributions approximately follow the theoretical distributions. Similar to DM halos, the NN-PDF peaks in smaller scales compared to the SC-PDF. Again, we conclude that the NN-PDF probes smaller scales in comparison with the SC-PDF which probes larger scales.

In Fig. 6 we plot the SC-CDF in panel (a) and the NN-CDF in panel (b) for galaxy groups. In panel (c), we plot the J-function where the samples are selected as $M_{r,\text{lim}} = -18, -19, -20$ (see Table (1)). We present these samples with a red circle, blue square and green

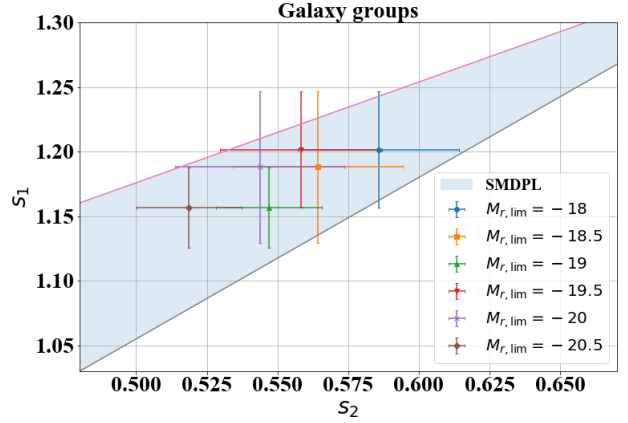


Figure 7. First moment of the SC-PDF for galaxy groups of the volume limited catalogue, s_1 in equation (19), is plotted for different magnitude limits with respect to a) s_2 . We show sample $M_{r,\text{lim}} = -18$ with the blue circle, $M_{r,\text{lim}} = -18.5$ with the orange square, $M_{r,\text{lim}} = -19$ with the green up-pointing triangle, $M_{r,\text{lim}} = -19.5$ with the red down-pointing triangle, $M_{r,\text{lim}} = -20$ with the purple and $M_{r,\text{lim}} = -20.5$ with the brown diamond. The result of Λ CDM halos from the SMDPL simulation by soft blue region.

triangle, respectively. The similarity of different samples within error bars can be deduced based on Fig. 6. Note that we do not consider any limit on the mass of the galaxy groups. So low mass and high mass groups are present in the volume-limited catalogues. This situation is comparable with the low mass dark matter halo samples of Section 3. In near future, the number of observed galaxy groups will increase. Accordingly, it would be possible to set additional conditions on the samples, such as dynamical mass limit. This can help us to break the degeneracy between different samples. We calculate moments of the SC-PDF in Table (5) and logarithmic moments of the NN-PDF in Table (6). In the column one of the tables, we present magnitude limit. In the rest of the four columns s_1, s_2, \tilde{s}_3 and \tilde{s}_4 are presented for the SC-PDF l_1, l_2, \tilde{l}_3 and \tilde{l}_4 for the NN-PDF. The errors on the moments are below 5% for the first and second moments. We should note that we consider conservative errors.

The SC-PDF skewness is around 0.5, and the NN-PDF has approximately 0.15 logarithmic skewness. (See the column four of the Tables (5,6)). Similar to the halos, the NN-PDF skewness is smaller than the SC-PDF and kurtosis of the SC-PDF is approximately between 3.2 and 3.4. On the other hand, logarithmic kurtosis of the NN-PDF is approximately between 2.5 and 2.7. This shows that the SC-PDF can be considered as a nearly normal distribution while the NN-PDF is nearly log-normal, which is consistent with Fig. 5 and the SMDPL simulation.

In Fig. 7 we plot s_1 with respect to s_2 for the 6 samples of Tables (5). Blue circle shows $M_{r,\text{lim}} = -18$, orange square shows $M_{r,\text{lim}} = -18.5$, green up-pointing triangle shows $M_{r,\text{lim}} = -19$, red down-pointing triangle shows $M_{r,\text{lim}} = -19.5$, purple x-symbol shows $M_{r,\text{lim}} = -20$ and brown diamond shows $M_{r,\text{lim}} = -20.5$. Soft blue region is extracted from the SMDPL which we plot it in Fig. 3. The moments derived from galaxy groups shows consistency with the soft blue region from the SMDPL. This result is compelling, considering the difference between samples of the dark matter halos of SMDPL simulation and the galaxy

Table 5. We report the moments of the SC-PDF for the samples of Table (4) calculated by equation (19). The condition on magnitude is presented in the column one. In the columns 3, 4, 5, 6 we report the quantities s_1 , s_2 , \tilde{s}_3 and \tilde{s}_4 , respectively.

$M_{r,\text{lim}}$	s_1	s_2	\tilde{s}_3	\tilde{s}_4
18	1.202 ± 0.045	0.586 ± 0.029	0.648 ± 0.07	3.264 ± 0.165
18.5	1.188 ± 0.059	0.564 ± 0.03	0.633 ± 0.056	3.324 ± 0.179
19	1.157 ± 0.031	0.547 ± 0.019	0.679 ± 0.066	3.457 ± 0.225
19.5	1.198 ± 0.045	0.558 ± 0.024	0.563 ± 0.049	3.12 ± 0.171
20	1.177 ± 0.037	0.544 ± 0.013	0.62 ± 0.044	3.262 ± 0.137
20.5	1.165 ± 0.035	0.519 ± 0.01	0.518 ± 0.128	3.159 ± 0.512

Table 6. The logarithmic moments of the NN-PDF related to the samples of Table (4) calculated by equation (19). The condition on magnitude is shown in column 1. In columns 3, 4, 5, 6 the quantities l_1 , l_2 , \tilde{l}_3 and \tilde{l}_4 are respectively represented.

$M_{r,\text{lim}}$	l_1	l_2	\tilde{l}_3	\tilde{l}_4
18	-0.672 ± 0.034	0.554 ± 0.018	0.242 ± 0.043	2.768 ± 0.126
18.5	-0.658 ± 0.027	0.56 ± 0.018	0.216 ± 0.042	2.728 ± 0.119
19	-0.658 ± 0.031	0.554 ± 0.009	0.157 ± 0.083	2.664 ± 0.091
19.5	-0.663 ± 0.024	0.561 ± 0.013	0.151 ± 0.048	2.679 ± 0.064
20	-0.679 ± 0.024	0.583 ± 0.015	0.107 ± 0.03	2.574 ± 0.046
20.5	-0.679 ± 0.027	0.618 ± 0.016	-0.013 ± 0.051	2.527 ± 0.047

groups catalogue. The volume-limited galaxy groups have the condition on their magnitudes, while the SMDPL halo samples have constrained on their masses. The uncertainties are substantial, both for simulation and observational data-sets. However, in light of precise future galaxy surveys (Amendola et al. 2018) and technological advances in numerical simulations (Adamek et al. 2016; Hassani et al. 2019), one could reduce the errors significantly. Thus a more precise comparison between the data and simulation will be available in near future.

5 CONCLUSIONS AND REMARKS

The standard model of cosmology is well tested in the last two decades in linear regime mainly, using two-point statistics. However, with the upcoming surveys going to observe the Universe in deeply non-linear regimes, the main challenge would be to compare the theory with observation in non-linear scales. In this work, we mainly focus on the idea of using complimentary statistical probes to study the non-linear scales. In non-linear scales, the matter distribution is far from Gaussian, and we can approximate it by a log-normal distribution. At these scales, study of the statistics that depend on higher-order correlation functions is experimentally and theoretically motivated. At first glance, they can improve constraints on the cosmological parameters from a given data. Moreover, the two other advantages of these functions are 1) Finding the universality behaviours. For example, the scaling relation for the void function gives information about the statistics of the matter density and the form of n -points correlation functions of halos/galaxies. 2) Finding differences between samples which leads us to extract more information in order to constrain the parameters and to distinguish cosmological models. For an example, breaking the degeneracy between bias and σ_8 parameters (Banerjee & Abel 2020).

In this work, we used the SMDPL simulation from the MultiDark project. Also, we use the galaxy groups from the volume-limited

Tempel catalogue. We calculated the Spherical Contact (SC) distribution function, Nearest Neighbour (NN) distribution function, and the J-function in simulations and observational data. We choose the dark matter halo samples from the SMDPL by introducing limits on mass and redshift. We use the galaxy group sample with limits on the magnitude.

Our results suggest that, the SC-CDF/PDF probes larger scales compared to the NN-CDF/PDF. Accordingly, the NN-CDF reveals difference between the samples. For specific mass scale, different redshifts have similar s_1 , l_1 but they have different s_2 , l_2 for the SC-PDF and NN-PDF respectively. We also obtain similar results for galaxy groups. Our main findings are summarised as follows:

- In both the SMDPL and galaxy groups, the SC-PDF distribution is nearly skew-normal and the NN-PDF is nearly log-normal. The NN-PDF is more sensitive to non-linear clustering than the SC-PDF. The non-unity of the J-function comes from the difference between the NN-PDF and SC-PDF.
- For a specific mass scale and different redshifts, first moments is the same for both the SC-PDF and NN-PDF. As a result, we can use second moments to distinguish between samples. However, the NN-CDF reveals the differences more clearly.
- In the SMDPL, for the SC-PDF, a linear relation between s_1 and s_2 is found. The results for the galaxy groups are also consistent with the SMDPL considering the error bars. Using a more precise approach of error finding and considering the simulations with larger box sizes, errors will be reduced significantly and we can compare the s_1 , s_2 relation between the simulations and data better. The relation between l_1 and l_2 is complicated and the trend changes in mass scales around $\sim 10^{12} M_\odot h$.
- We find the first two moments of the SC-PDF/NN-PDF for galaxy groups within 5 percent errors.
- Some samples are similar in their SC-CDF but have different NN-CDF. This suggests a complementary role of the SC-CDF and NN-CDF and show that they contain different information.
- The J-function is equal to the first conditional correlation. It contains information about clustering. We calculated the J-function

for all the samples, and showed that it is sensitive to mass scale under consideration. In the larger mass scales, we have less clustering as their J-function is closer to one.

For future remarks, note that we usually test cosmological models to find the best fit of the parameters. This is not easily feasible at non-linear scales. However, our results suggest a possible intrinsic length scale in the form of the first moment of the SC-PDF. Due to our findings in this work, the first moments of the SC-PDF is redshift independent. The universality of the SC-CDF and the redshift independency could be a promising result to define a standard length scale for non-linear regime. In future work, we plan to study the universality of the J-function, which is a result of the scale-invariant correlation function. Finding the standard lengths from non-linear structures are important and they can be used as a ruler and they potentially can reveal tensions between distinct data sets. For example, finding a new standard ruler can be used to study H_0 tension (Riess et al. 2019). We also can search for cosmological models which breaks the universality or similarity. To compare results from simulation and observation more precisely we need to consider baryoninc effects, which is subject of future works.

ACKNOWLEDGEMENTS

We are grateful to Ali Akbar Abolhassani, Julian Adamek, Jean-Pierre Eckmann, Nima Khosravi, Martin Kunz, David Mota, Sohrab Rahvar, and Saeed Tavasoli, for many fruitful discussions and insightful comments on the manuscript. SB is partially supported by Abdus Salam International Center of Theoretical Physics (ICTP) under the junior associateship scheme. This research is supported by Sharif University of Technology Office of Vice President for Research under Grant No. G960202.

The CosmoSim database used in this paper is a service by the Leibniz-Institute for Astrophysics Potsdam (AIP). The MultiDark database was developed in cooperation with the Spanish MultiDark Consolider Project CSD2009-00064

The computations were performed at University of Geneva on the Baobab and Yggdrasil clusters. Part of the computations for this paper were performed on the Euclid Cluster at the Institute of Theoretical Astrophysics at University of Oslo.

DATA AVAILABILITY

In this paper, we used data from the Small Multidark Planck simulation³. The FOF halo catalogs are available at the CosmoSim database (<https://www.cosmosim.org/cms/simulations/smdpl/>). For the observational section, we used the Tempel 2014 galaxy catalogues from the CosmoDB database (http://cosmodb.to.ee/cms/documentation/sdss_dr10/). Both data sets are open source and reachable for the community. The codes are available under request.

REFERENCES

- Abbott T. M. C., et al., 2018, *Phys. Rev. D*, 98, 043526
Adamek J., Daverio D., Durrer R., Kunz M., 2016, *JCAP*, 07, 053
Ade P. A. R., et al., 2014, *Astron. Astrophys.*, 571, A16

- Aghanim N., et al., 2020, *Astron. Astrophys.*, 641, A6
Agustsson I., Brainerd T. G., 2018, *Astrophys. J.*, 862, 169
Ahn C. P., et al., 2014, *Astrophys. J. Suppl.*, 211, 17
Akrami Y., et al., 2020, *Astron. Astrophys.*, 641, A10
Alam S., et al., 2017, *Mon. Not. Roy. Astron. Soc.*, 470, 2617
Amendola L., et al., 2018, *Living Rev. Rel.*, 21, 2
Appleby S., Park C., Hong S. E., Kim J., 2018, *Astrophys. J.*, 853, 17
Baddeley A., Bárány I., Schneider R., 2006, *Stochastic Geometry: Lectures*
Given at the CIME Summer School Held in Martina Franca, Italy, September 13-18, 2004. Springer
Baghran S., Afshordi N., Zurek K. M., 2011, *Phys. Rev. D*, 84, 043511
Balian R., Schaeffer R., 1989, *Astronomy and Astrophysics*, 220, 1
Banerjee A., Abel T., 2020, *Mon. Not. Roy. Astron. Soc.*, 500, 5479
Banerjee A., Abel T., 2021, arXiv preprint arXiv:2102.01184
Bernardeau F., 1992, *The Astrophysical Journal*, 392, 1
Bernardeau F., Colombi S., Gaztanaga E., Scoccimarro R., 2002, *Phys. Rept.*, 367, 1
Bernardeau F., Pichon C., Codis S., 2014, *Phys. Rev. D*, 90, 103519
Chiu S. N., Stoyan D., Kendall W. S., Mecke J., 2013, *Stochastic geometry and its applications*. John Wiley & Sons
Clark P. J., Evans F. C., 1954, *Ecology*, 35, 445
Coles P., Jones B., 1991, *Monthly Notices of the Royal Astronomical Society*, 248, 1
Colley W. N., Gott J. R., 2015, *Mon. Not. Roy. Astron. Soc.*, 447, 2034
Colombi S., 1994, *Astrophys. J. Lett.*, 435, L536
Croton D. J., et al., 2004, *Mon. Not. Roy. Astron. Soc.*, 352, 828
Einasto J., H tsi G., Liivam gi L., Einasto M., 2020, arXiv preprint arXiv:2011.13292
Fard M. A., Baghran S., 2018, *JCAP*, 01, 051
Feldmann R., Spolyar D., 2015, *Mon. Not. Roy. Astron. Soc.*, 446, 1000
Friedrich O., Uhlemann C., Villaescusa-Navarro F., Baldauf T., Manera M., Nishimichi T., 2020, *Mon. Not. Roy. Astron. Soc.*, 498, 464
Fry J. N., 1986, *ApJ*, 306, 358
Fry J. N., Colombi S., 2013, *Mon. Not. Roy. Astron. Soc.*, 433, 581
Gaztanaga E., Fosalba P., Elizalde E., 2000, *The Astrophysical Journal*, 539, 522
Got III J. R., Choi Y.-Y., Park C., Kim J., 2008, arXiv preprint arXiv:0812.1406
Gott III J. R., Melott A. L., Dickinson M., 1986, *The Astrophysical Journal*, 306, 341
Guth A. H., 1981, *Physical Review D*, 23, 347
Hamilton A., Gott III J. R., Weinberg D., 1986, *The Astrophysical Journal*, 309, 1
Hassani F., Adamek J., Kunz M., Vernizzi F., 2019, *JCAP*, 12, 011
Hinshaw G., et al., 2013, *The Astrophysical Journal Supplement Series*, 208, 19
Hubble E. P., 1936, *Realm of the Nebulae*
Ivanov M. M., Kaurov A. A., Sibiryakov S., 2019, *JCAP*, 03, 009
Ivanov M. M., Simonovi  M., Zaldarriaga M., 2020, *Journal of Cosmology and Astroparticle Physics*, 2020, 042
Jamieson D., Loverde M., 2020, *Phys. Rev. D*, 102, 123546
Kerscher M., Pons-Borderia M. J., Schmalzing J., Trasarti-Battistoni R., Buchert T., Martinez V. J., Valdarnini R., 1999, *Astrophys. J.*, 513, 543
Klypin A., Prada F., Betancort-Rijo J., Albareti F. D., 2018, *Mon. Not. Roy. Astron. Soc.*, 481, 4588
Lacey C., Cole S., 1994, *Monthly Notices of the Royal Astronomical Society*, 271, 676
Lam T. Y., Sheth R. K., 2008, *Monthly Notices of the Royal Astronomical Society*, 386, 407
Li F., Erickcek A. L., Law N. M., 2012, *Phys. Rev. D*, 86, 043519
Linde A. D., 1982, *Physics Letters B*, 108, 389
Mandal A., Nadkarni-Ghosh S., 2020, *Monthly Notices of the Royal Astronomical Society*, 498, 355
Martinez V. J., Saar E., 2001, *Statistics of the galaxy distribution*. CRC press
Maugerordato S., Lachize-Rey M., 1987, *The Astrophysical Journal*, 320, 13
Maugerordato S., Lachize-Rey M., 1991, *ApJ*, 369, 30
Melott A. L., 1990, *Physics Reports*, 193, 1

³ doi:10.17876/cosmosim/smdpl/

- Munshi D., Bernardeau F., Melott A., Schaeffer R., 1999, *Monthly Notices of the Royal Astronomical Society*, 303, 433
- Paranjape A., Alam S., 2020, *Mon. Not. Roy. Astron. Soc.*, 495, 3233
- Rahvar S., Baghran S., Afshordi N., 2014, *Phys. Rev. D*, 89, 063001
- Repp A., Szapudi I., 2020a, *Mon. Not. Roy. Astron. Soc.*, 498, L125
- Repp A., Szapudi I., 2020b, *Mon. Not. Roy. Astron. Soc.*, 500, 3631
- Riebe K., et al., 2013, *Astronomische Nachrichten*, 334, 691
- Riess A. G., Casertano S., Yuan W., Macri L. M., Scolnic D., 2019, *The Astrophysical Journal*, 876, 85
- Sanchez A. G., et al., 2012, *Mon. Not. Roy. Astron. Soc.*, 425, 415
- Schmalzing J., Buchert T., 1997, *Astrophys. J. Lett.*, 482, L1
- Scoccimarro R., Colombi S., Fry J. N., Frieman J. A., Hivon E., Melott A., 1998, *The Astrophysical Journal*, 496, 586
- Sefusatti E., Crocce M., Pueblas S., Scoccimarro R., 2006, *Physical Review D*, 74, 023522
- Sharp N. A., 1981, *Monthly Notices of the Royal Astronomical Society*, 195, 857
- Shi F., et al., 2016, *The Astrophysical Journal*, 833, 241
- Shin J., Kim J., Pichon C., Jeong D., Park C., 2017, *The Astrophysical Journal*, 843, 73
- Soneira R. M., Peebles P., 1977, *The Astrophysical Journal*, 211, 1
- Szapudi I., Szalay A. S., 1993, *The Astrophysical Journal*, 408, 43
- Tempel E., et al., 2014, *Astronomy & Astrophysics*, 566, A1
- Ueda H., Yokoyama J., 1996, *Monthly Notices of the Royal Astronomical Society*, 280, 754
- Uhlemann C., Codis S., Pichon C., Bernardeau F., Reimberg P., 2016, *Monthly Notices of the Royal Astronomical Society*, 460, 1529
- Uhlemann C., Friedrich O., Villaescusa-Navarro F., Banerjee A., Codis S., 2020, *Monthly Notices of the Royal Astronomical Society*, 495, 4006
- Van Lieshout M., Baddeley A., 1996, *Statistica Neerlandica*, 50, 344
- Verde L., Heavens A. F., 2001, *Astrophys. J.*, 553, 14
- Walsh K., Tinker J., 2019, *Mon. Not. Roy. Astron. Soc.*, 488, 470
- Wang X., Chen X., Park C., 2012, *The Astrophysical Journal*, 747, 48
- Wang Y., Brunner R., Dolence J., 2013, *Monthly Notices of the Royal Astronomical Society*, 432, 1961
- White S. D., 1979, *Monthly Notices of the Royal Astronomical Society*, 186, 145
- York D. G., et al., 2000, *The Astronomical Journal*, 120, 1579
- Zunckel C., Gott III J. R., Lunnan R., 2011, *Monthly Notices of the Royal Astronomical Society*, 412, 1401
- Zwicky F., 1957, *Publications of the Astronomical Society of the Pacific*, 69, 518
- de Martino I., Chakrabarty S. S., Cesare V., Gallo A., Ostorero L., Diaferio A., 2020, *Universe*, 6, 107

APPENDIX A: UNIVERSALITY OF THE VOID PROBABILITY FUNCTION

The relation between the SC-CDF and the NN-CDF to cosmological parameters and initial conditions is complicated. In this direction, universal features of non-linear matter density help us extract information from deeply non-linear scales. For example, [White \(1979\)](#) proposed a scaling relation for the void probability (VP) function. In this section, we review the universality of the VP function. It results in a universal form for $\ln P_0/nV$. We also find a similarity for the first moments of the SC-PDF in different redshifts. We follow [Balian & Schaeffer \(1989\)](#) and show the scaling relations from equation (4), while assuming a scale invariant n -point correlation function as,

$$\xi_N(\mathbf{r}_1, \dots, \mathbf{r}_N) = \lambda^{-(N-1)\gamma} \xi(\mathbf{r}_1, \dots, \mathbf{r}_N), \quad (\text{A1})$$

where γ is a constant. This form of n -point correlation function has a theoretical and observational motivation ([Bernardeau et al. 2002](#)). The scale invariant assumption, as well as the transitional

and rotational symmetry leads to the following power-law relation for the two-point correlation function

$$r^\gamma \xi_2(r) = \text{constant}. \quad (\text{A2})$$

Averaging over volume V leads to a similar equation for the averaged two-point correlation function

$$V^{\gamma/3} \int \frac{1}{V^2} \xi_2(\mathbf{r}_1, \mathbf{r}_2) dV_1 dV_2 = V^{\gamma/3} \bar{\xi}_2 = \text{constant}. \quad (\text{A3})$$

It is straightforward to show that the scale invariance assumption results in a scaling relation for the conditional correlation function Ξ_i , equation (2)

$$\Xi_i(\mathbf{r}_1, \dots, \mathbf{r}_i; V) = \sum_j \frac{(-nV)^j}{j!} (\bar{\xi}_2)^{i+j-1} S_{i,j}(\mathbf{r}_1, \dots, \mathbf{r}_i), \quad (\text{A4})$$

in which $S_{i,j}$ is

$$S_{i,j}(\mathbf{r}_1, \dots, \mathbf{r}_i) = \int \xi_{i+j}((\bar{\xi}_2)^{1/\gamma} \mathbf{r}_1, \dots, (\bar{\xi}_2)^{1/\gamma} \mathbf{r}_{i+j}) \frac{dV_{i+1}}{V} \dots \frac{dV_{i+j}}{V}. \quad (\text{A5})$$

Then we show that $S_{i,j}$ is independent of volume and $\bar{\xi}_2$. In this case, the quantity $(nV)^{i-1} \Xi_i$ is a universal function of $nV\bar{\xi}_2$ and so different samples exhibit similar behaviour with respect to $nV\bar{\xi}_2$. Finally, the observational quantities e.g., $\ln P_0/(nV)$, which is equal to $\Xi_0/(nV)$ (see equation (4)), is treated as a universal function of $nV\bar{\xi}_2$. However, the universality happens only if $S_{i,j}$ is independent of volume V , the averaged two point correlation function $\bar{\xi}_2$ and also \mathbf{r}_i for $i > 0$. This argument is intuitively grasped when we apply a changing variables as $d^3\rho_j = \frac{dV_j}{V}$. By this definition, in equation (A5) the integrals are taken over spheres with radius of unity length and we have

$$S_{i,j}(\rho_1, \dots, \rho_i) = \int \xi_{i+j}(c\rho_1, \dots, c\rho_{i+j}) d^3\rho_{i+1} \dots d^3\rho_{i+j}, \quad (\text{A6})$$

where $c = (\bar{\xi}_2)^{1/\gamma} V^{1/3}$ is a constant using equation (A3). [Balian & Schaeffer \(1989\)](#) examined the universality of $S_{0,j}$. For $S_{i,j}$ the arguments might not hold anymore. Finding an exact solution for $S_{i,j}$ is out of the scope of this work.

([Croton et al. 2004](#)) investigated the universality of $\ln P_0/(nV)$, and they proposed negative binomial function as a good approximation for this function in

$$\ln P_0/(nV) = \frac{1}{nV\bar{\xi}_2} (1 + \ln(nV\bar{\xi}_2)). \quad (\text{A7})$$

Employing equation (7), we see that the J-function is equal to Ξ_1 . It suggests that J-function is also a universal function.

In the following, we focus on variable $nV\bar{\xi}_2$. $\bar{\xi}_2$ calculated by equation

$$\bar{\xi}_2 = \frac{\langle N^2 \rangle - \langle N \rangle^2 - \langle N \rangle}{\langle N \rangle^2}, \quad (\text{A8})$$

where $\sqrt{\langle N^2 \rangle - \langle N \rangle^2}$ is the standard deviation of number count probability of the volume V . $\langle N \rangle$ is the mean number of particles found in volume V , which is equal to nV . In literature $\bar{N} \equiv nV$ is defined instead of r variable ([Fry & Colombi 2013](#)). However, we mainly focus on the length scales. We redefine $x^3 \equiv (\frac{4\pi}{3}n)r^3$ in which $V = 4\pi/3r^3$ and throughout this work we investigate x (dimensionless variable) dependency of the SC-CDF, the NN-CDF, and the J-function. Finally, we mention that we find similarity for the VP function versus dimensionless variable x and not the well-known

parameter $x\tilde{\xi}_2$. This argument suggests a new form of universality in redshifts, which we will investigate in future works with more details.

APPENDIX B: COMPARING THE TWO SIMULATIONS: MDPL AND MDPL2

In this appendix, we discuss the results of the other simulations of the "MultiDark" project (Riebe et al. 2013). Especially the MDPL and MDPL2. They are similar to SMDPL but with a larger box size of 1 Gp/h. The MDPL and MDPL2 are different in their seed numbers. So in this section, we discuss the effect of the box size and the initial conditions. Here, similar to Section 3, we estimate the errors conservatively, where we divide the main box into 27 sub-boxes. We also present our approach to the error estimation in this appendix.

In Fig. B1 we plot in panels (a) $F(x)$, (b) $G(x)$, and (c) $J(x) = \frac{1-G(x)}{1-F(x)}$ as a function of $x = \sqrt[3]{nV}$. In this figure, the mass limit is $M > 10^{12} M_\odot h$ and $z = 0$. Since the box size of the MDPL and MDPL2 simulations are larger, the error bars are smaller and barely recognisable in the figures. The red circles are for the SMDPL, for MDPL we use blue square, and the green triangles are for the MDPL2. Figures show good agreement between the same samples in different simulations.

In Fig. B2 we plot in panel (a) s_1 as a function of s_2 , for the SC-PDF and in panel (b) l_1 as a function of l_2 , for the NN-PDF. In this figure, we only consider the case $z = 0$, and the different points are related to different mass scales, $\log(M_{\text{lim}}/M_\odot h) = \{12, 12.5, 13, 13.5, 14\}$. In Fig. B2 moments of the SC-PDF is similar in the different simulations, which were predictable as the functions are independent of the box size. It is also true for moments of the NN-PDF. Except to the mass scale above $10^{12} M_\odot h$. For this mass scale s_1 is -0.649 ± 0.010 for the SMDPL, -0.668 ± 0.003 for the MDPL and -0.666 ± 0.005 for the MDPL2. MDPL and MDPL2 agree. However, they are far from SMDPL results within one sigma confidence level. An explanation is systematic from boundary effects Chiu et al. (2013). In these scales, The statistical errors are small and comparable to the systematic errors. In the MDPL and the MDPL2, the number of halos is large, and the errors are negligible.

To find the statistical errors, we divided each simulation box into different sub-boxes and reported the variance as an error. Accordingly, we divide the MDPL to 10^3 and the SMDPL to 4^3 sub-boxes. We plot the PDF of the logarithmic mean of the NN-PDF, l_1 in Fig. B3. We choose the sub-samples to have 100 Mpc/h lengths for both the MDPL and the SMDPL. In this figure, we plot the normal fitting distributions with dashed yellow for MDPL. The dot-dashed green line is for the SMDPL. The plot ensures the errors are Gaussian. Also, results from the MDPL and the SMDPL agree with each other.

We conclude that the seed number does not change the functions. The SC-PDF does not depend on the box size, and importantly, the same linear relation between s_1 and s_2 exist for the other simulations. In large-box simulations and small mass scales, the number of halos is large, so the statistical errors are comparable with systematic errors.

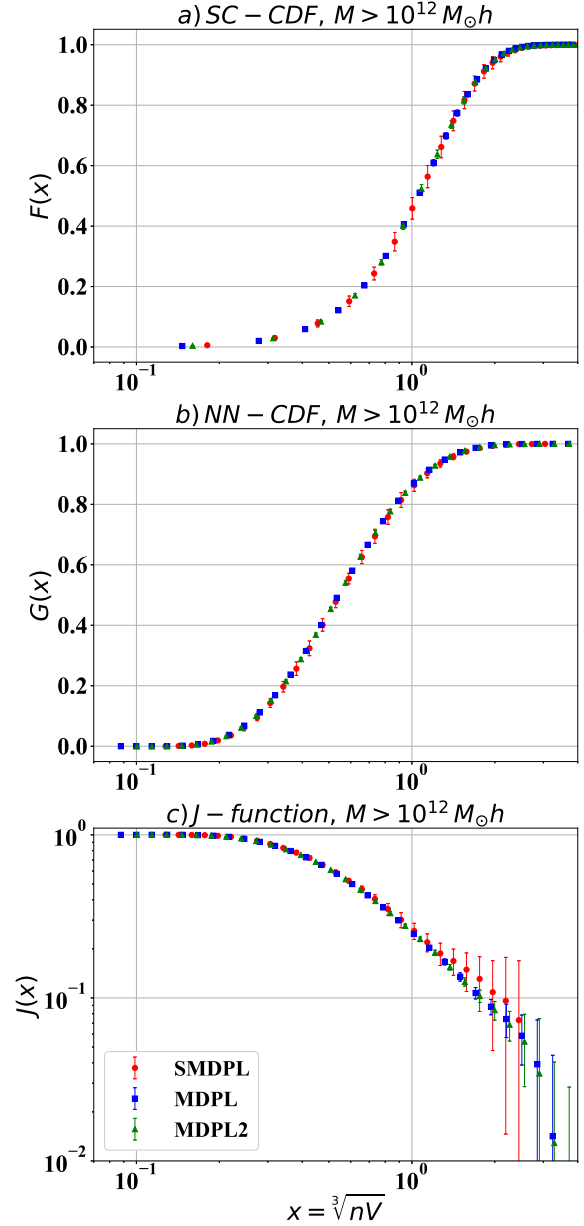


Figure B1. We plot in panel (a) $F(x)$, SC-CDF, (b) $G(x)$, NN-CDF and (c) $J(x) = \frac{1-G(x)}{1-F(x)}$ with respect to $x = \sqrt[3]{nV}$ for DM halos from simulation. Mass limit is $10^{12} M_\odot h$ and $z = 0$. Red circles represent the SMDPL simulation, blue squares correspond to MDPL and green triangles are for MDPL2.

APPENDIX C: GENERAL BEHAVIOUR OF THE SC-PDF AND THE NN-PDF

As we discussed in the main text, we focus on the normal and log-normal distributions as indicators of the linear and non-linear scales. We calculated the moments of the SC-PDF in Table (2) and the log-moments of the NN-PDF in Table (3). We showed that the SC-PDF and the NN-PDF follow approximately the normal and log-normal distribution, respectively. However, we can ask the question vice versa. What about the log-moments of the SC-PDF and moments of the NN-PDF? Note that the kurtosis of the normal distribution is three. We use this property to distinguish the normal and log-normal

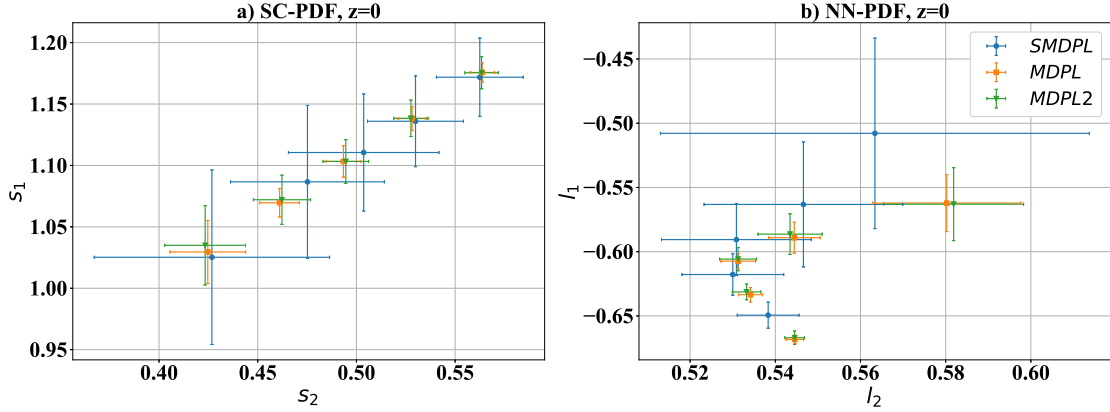


Figure B2. The panel (a) s_1 with respect to s_2 and (b) l_1 with respect to l_2 is plotted for dark matter halos from different simulations. The blue circle is for the SMDPL, orange square is for MDPL, green triangle is for MDPL2. Points represent the mass limits $\log(M_{\text{lim}}/M_{\odot}h) = \{12, 12.5, 13, 13.5, 14\}$.

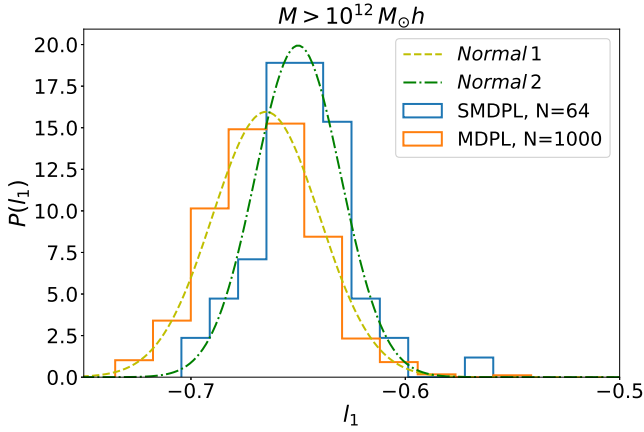


Figure B3. The NN-PDF logarithmic mean, l_1 is plotted for different sub-boxes. The SMDPL simulation with 64 sub-boxes is plotted in blue, and the MDPL simulation with 1000 sub-boxes in a solid orange line. The estimated normal distributions are plotted with dot-dashed green and dashed yellow lines, respectively.

distributions. In this appendix, we show that the NN-PDF, due to its large kurtosis, is far from a normal distribution. For the SC-PDF the kurtosis of the normal and log-normal distribution is almost the same regarding the confidence level. In Tables (C1),(C2), we calculate the logarithmic moments of the SC-PDF and the moments of the NN-PDF. Noting column four of Table (C1), the log-kurtosis \tilde{l}_4 is larger than 3.9 for all the cases except the large mass case. We can compare this number with column four of Table (2), in which the kurtosis of the SC-PDF, \tilde{s}_4 , is smaller than 3.9 for all cases. However, considering errors, for most cases, two numbers overlap. So there is an opportunity to approximate the SC-PDF with a logarithmic distribution. The situation is more clear for NN-PDF. Comparing column four between Table (C2) and Table (3), log-kurtosis is around 2.6 but range of kurtosis is from 8.2 to 2.1. So NN-PDF is nearly log-normal can't be approximated with a normal distribution.

In Fig. C1, we plot the kurtosis and log-kurtosis corresponding to halos from the SMDPL. We present the SC-PDF in panel (a) and

the NN-PDF in panel (b). In the figure, the blue circles show $z = 0$ (\tilde{s}_4), orange squares show $z = 1$ (\tilde{s}_4), green down-pointing triangle show $z = 0$ (\tilde{l}_4) and red up-pointing triangle show $z = 1$ (\tilde{l}_4). (again, similar to Fig. 3, we shifted mass scales slightly for clarity). The situation for the NN-PDF is certain when the logarithmic kurtosis deviates from the normal kurtosis completely. For the SC-PDF for scales (10^{11} and 10^{12}), \tilde{s}_4 is lower than \tilde{l}_4 and it is closer to three comparing to \tilde{l}_4 . For the other mass limits, considering the error bars, we can not distinguish the two classes. However, considering mean kurtosis, for all cases, \tilde{s}_4 is lower than \tilde{l}_4 . Accordingly, in the main text, we report that the SC-PDF is a nearly normal distribution.

This paper has been typeset from a \LaTeX file prepared by the author.

Table C1. The logarithmic moments of the SC-PDF related to samples of Table (1) calculated by equation (19). The condition on mass and redshift is presented in columns one and two, respectively. l_1 , l_2 , \tilde{l}_3 and \tilde{l}_4 are reported in following columns.

$\log(M_{\text{lim}}/M_{\odot}h)$	redshift(z)	l_1	l_2	\tilde{l}_3	\tilde{l}_4
11	0	0.091 ± 0.019	0.569 ± 0.004	-0.703 ± 0.02	3.907 ± 0.059
11	0.5	0.082 ± 0.018	0.565 ± 0.003	-0.717 ± 0.021	3.957 ± 0.068
11	1	0.079 ± 0.018	0.561 ± 0.004	-0.729 ± 0.021	3.958 ± 0.065
11.5	0	0.059 ± 0.021	0.554 ± 0.005	-0.735 ± 0.025	3.979 ± 0.085
11.5	0.5	0.053 ± 0.022	0.549 ± 0.005	-0.745 ± 0.03	4.009 ± 0.122
11.5	1	0.054 ± 0.022	0.546 ± 0.003	-0.756 ± 0.032	4.015 ± 0.103
12	0	0.029 ± 0.026	0.541 ± 0.007	-0.768 ± 0.043	4.04 ± 0.154
12	0.5	0.028 ± 0.025	0.536 ± 0.006	-0.781 ± 0.052	4.089 ± 0.238
12	1	0.029 ± 0.025	0.531 ± 0.006	-0.81 ± 0.049	4.187 ± 0.242
12.5	0	0.004 ± 0.03	0.528 ± 0.011	-0.815 ± 0.095	4.284 ± 0.475
12.5	0.5	0.004 ± 0.028	0.523 ± 0.011	-0.825 ± 0.092	4.26 ± 0.522
12.5	1	0.006 ± 0.035	0.519 ± 0.013	-0.849 ± 0.113	4.267 ± 0.415
13	0	-0.012 ± 0.042	0.513 ± 0.017	-0.82 ± 0.161	4.228 ± 0.613
13	0.5	-0.014 ± 0.038	0.504 ± 0.021	-0.831 ± 0.173	4.244 ± 1.005
13	1	-0.005 ± 0.048	0.501 ± 0.021	-0.929 ± 0.198	4.613 ± 1.063
13.5	0	-0.028 ± 0.061	0.498 ± 0.034	-0.873 ± 0.247	4.518 ± 1.255
13.5	0.5	-0.043 ± 0.052	0.489 ± 0.036	-0.847 ± 0.159	3.983 ± 0.79
13.5	1	-0.05 ± 0.073	0.47 ± 0.049	-0.778 ± 0.323	3.947 ± 1.462
14	0	-0.08 ± 0.074	0.48 ± 0.055	-0.875 ± 0.432	4.157 ± 1.542
14	0.5	-0.071 ± 0.096	0.471 ± 0.096	-0.857 ± 0.588	3.918 ± 2.151
14	1	-0.133 ± 0.145	0.41 ± 0.149	-0.476 ± 0.648	2.907 ± 1.132

Table C2. The moments of the NN-PDF related to the samples of Table (1) calculated by equation (19). The condition on mass and redshift are presented in columns one and two respectively. s_1 , s_2 , \tilde{s}_3 and \tilde{s}_4 are reported in following columns.

$\log(M_{\text{lim}}/M_{\odot}h)$	redshift(z)	s_1	s_2	\tilde{s}_3	\tilde{s}_4
11	0	0.566 ± 0.007	0.347 ± 0.007	1.82 ± 0.035	8.253 ± 0.301
11	0.5	0.567 ± 0.006	0.345 ± 0.007	1.832 ± 0.04	8.228 ± 0.347
11	1	0.563 ± 0.006	0.345 ± 0.007	1.862 ± 0.034	8.28 ± 0.264
11.5	0	0.586 ± 0.007	0.347 ± 0.008	1.703 ± 0.046	7.458 ± 0.326
11.5	0.5	0.585 ± 0.007	0.346 ± 0.008	1.741 ± 0.055	7.608 ± 0.457
11.5	1	0.579 ± 0.007	0.348 ± 0.008	1.754 ± 0.049	7.468 ± 0.341
12	0	0.604 ± 0.008	0.347 ± 0.009	1.589 ± 0.082	6.831 ± 0.612
12	0.5	0.601 ± 0.008	0.348 ± 0.01	1.633 ± 0.08	6.892 ± 0.673
12	1	0.592 ± 0.01	0.353 ± 0.011	1.642 ± 0.061	6.71 ± 0.404
12.5	0	0.621 ± 0.012	0.35 ± 0.015	1.511 ± 0.096	6.254 ± 0.708
12.5	0.5	0.617 ± 0.012	0.357 ± 0.014	1.555 ± 0.11	6.305 ± 0.701
12.5	1	0.604 ± 0.015	0.366 ± 0.015	1.544 ± 0.099	6.121 ± 0.647
13	0	0.639 ± 0.021	0.36 ± 0.022	1.442 ± 0.135	5.681 ± 0.794
13	0.5	0.638 ± 0.023	0.375 ± 0.022	1.459 ± 0.15	5.705 ± 0.995
13	1	0.625 ± 0.03	0.39 ± 0.03	1.341 ± 0.234	5.086 ± 1.609
13.5	0	0.662 ± 0.035	0.378 ± 0.032	1.319 ± 0.271	5.095 ± 1.536
13.5	0.5	0.655 ± 0.049	0.385 ± 0.035	1.171 ± 0.293	4.423 ± 1.615
13.5	1	0.664 ± 0.057	0.425 ± 0.046	1.088 ± 0.341	3.977 ± 1.227
14	0	0.705 ± 0.053	0.399 ± 0.047	1.119 ± 0.424	4.356 ± 1.94
14	0.5	0.718 ± 0.082	0.423 ± 0.055	0.854 ± 0.381	3.341 ± 1.117
14	1	0.772 ± 0.165	0.435 ± 0.105	0.363 ± 0.559	2.138 ± 0.833

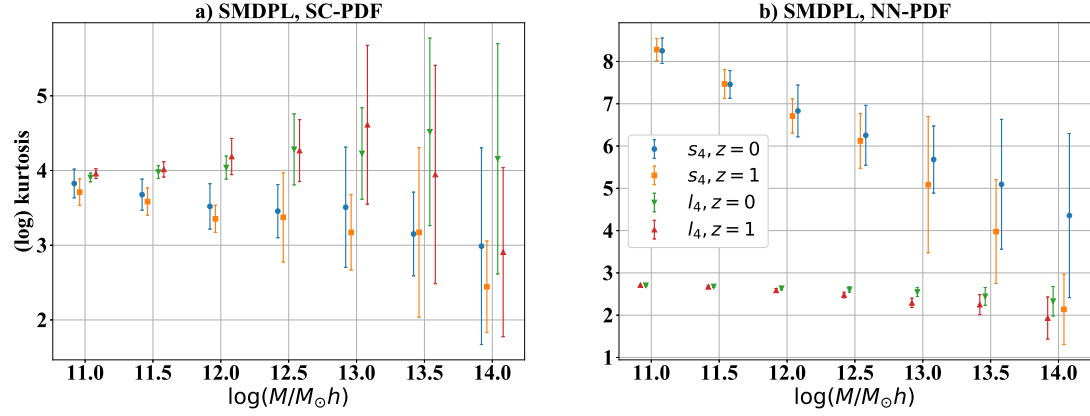


Figure C1. Kurtosis and logarithmic kurtosis of both (a) the SC-PDF and (b) the NN-PDF are plotted for SMDPL simulation versus mass scale. \tilde{s}_4 is plotted with blue circles for $z = 0$ and orange squares show $z = 1$. Also \tilde{l}_4 is plotted with green down-pointing triangle for $z = 0$ and red up-pointing triangle for $z = 1$. Mass scales are shifted slightly for clarity.